Chinese Journal of Chemical Engineering 87 (2025) 323–334

Contents lists available at ScienceDirect

Chinese Journal of Chemical Engineering

journal homepage: www.elsevier.com/locate/CJChE

Full Length Article

# Mechanisms governing coal ash fusion temperature by phosphorus

Guoyang Gui [1], Facun Jiao [1, 2, 3, *], Zhongbing Dong [1], Yunhu Hu [4], Shengtao Gao [1], Tao Liu [1], Yuanchun Zhang [1], Lirui Mao [1], Chengli Wu [1], Hanxu Li [1, 3]

[1] School of Chemical and Blasting Engineering, Anhui University of Science and Technology, Huainan 232001, China
[2] Engineering Technology Research Center of Coal Resources Comprehensive Utilization, Anhui University of Science and Technology, Huainan 232001, China
[3] Anhui Provincial Institute of Modern Coal Processing Technology, Anhui University of Science and Technology, Huainan 232001, China
[4] School of Chemistry and Materials Engineering, Huainan Normal University, Huainan 232001, China

ARTICLE INFO

*Article history:*
Received 25 February 2025
Received in revised form
3 May 2025
Accepted 11 June 2025
Available online 5 August 2025

*Keywords:*
Waste treatment
Gasification
Thermodynamics
Ash fusion temperature
Phosphorus
Dissolution of mullite

ABSTRACT

High phosphorus content in sewage sludge (SS) significantly affects the ash fusion temperature during the co-gasification of coal with SS. However, the mechanisms underlying the effects of phosphorus on the ash melting behavior remain unclear. In particular, there is no direct evidences to confirm that refractory mineral dissolution processes are affected by the phosphorus-bearing liquid phase formed during the initial stage of ash melting. In this study, different amount of calcium- and iron-phosphates were added to coal to investigate the effect of phosphorus on the coal ash fusion temperature. The phosphorus and mineral phase transformations, as well as the dissolution processes of refractory mullite particles in the phosphorus-bearing liquid phase, were determined using X-ray photoelectron spectroscopy, X-ray diffraction analysis, thermodynamic equilibrium calculations, and thermal platform microscope systems. The results indicated that the addition of 8% calcium-phosphate and iron-phosphate reduced the ash flow temperature (FT) from above 1500 °C to 1336°C and 1261 °C, respectively. The effect of iron-phosphate on the reduction of ash FT was more pronounced than that of calcium-phosphate. The phosphorus vaporization ratio increased with the temperature. Approximately 50% of phosphorus was retained in the samples to which 8% of calcium-phosphate and iron-phosphate were added at 1400 °C. Elevation of the temperatures promoted the conversion of $PO_4^{3-}$ to molten slag-dissolved $P_2O_5$. The mechanism whereby phosphorus reduces the ash FT is primarily governed by the dissolution of refractory minerals in the liquid phase formed during the initial heating stage. This dissolution process was enhanced in the presence Fe compared to that in the presence of Ca.


## 1. Introduction

Sewage discharge in China has increased with the acceleration of urbanization [1]. Sewage sludge (SS) an important byproduct of wastewater treatment contains approximately 80% water, organic matter, and toxic pathogens, posing a significant challenge for its treatment [2,3]. The production of SS in China reached 11.2 Mt (dry base) in 2022 [4]. Common treatment methods include landfilling, composting, land application, and thermal treatment. Among these methods, thermal treatment offers advantages such as pathogen elimination, heat recovery, and high treatment capacity [5–7]. Co-gasification with coal is a promising method for treating SS cleanly and efficiently [8–10].

Entrained-flow gasification, which is used to produce various chemicals, is a widely used technology for the clean conversion of coal into syngas. In this process, coal is converted into syngas within the gasifier, while the minerals in the coal transform into molten slag at high temperatures and are discharged from the bottom outlet of the gasifier [11–13]. The coal-ash fusion temperature is a crucial indicator for assessing the smoothly discharge of molten ash from the gasifier. Compared with coal, SS contains a higher phosphorus content, along with silicon, aluminum, calcium, iron, and other elements. These concentrations are often 10–1000 times higher than those in coal [5,7,14]. When SS is co-gasified with coal, phosphorus enters the slag, which influences the ash melting temperature. Numerous studies have focused on the impact of phosphorus on the ash melting characteristics

* Corresponding author.
*E-mail address:* fcjiao@aust.edu.cn (F. Jiao).

https://doi.org/10.1016/j.cjche.2025.06.014

[15–18]. Zhang *et al.* [19] investigated the effects of *P*-based additives (ammonium phosphate and calcium phosphate) on the melting characteristics of high-sodium coal ash under gasification conditions. Their results indicated that phosphorus has a high affinity for alkali and alkaline earth metals, resulting in the formation of high-melting-point phosphorus-containing minerals such as $Ca_9MgNa(PO_4)_7$, $Ca_9Fe(PO_4)_7$, and $Na_3Ca_6(PO_4)_5$. Zhang *et al.* [14] examined the influence of phosphorus on ash melting characteristics during the co-gasification of SS with coal. They found that the role of phosphorus in the melting temperature of coal ash largely depends on the $Al_2O_3/(CaO + Na_2O + K_2O)$ (A/CNK) molar ratio in the coal ash. When the A/CNK ratio was <1, phosphorus tended to react with Ca to form calcium-bearing refractory minerals. Conversely, when the A/CNK ratio was >1, phosphorus primarily existed in the amorphous phase, which reduced the ash fusion temperature. Wu *et al.* [15] investigated the effects of $P_2O_5$ on the melting temperature of coal ash. They found that when the $Al_2O_3/CaO$ ratio was low, the addition of $P_2O_5$ initially decreased the ash melting temperature, then increased it, and finally decreased it. However, when the $Al_2O_3/CaO$ ratio increased, the ash fusion temperature gradually decreased. Compared with silica, $P_2O_5$ has a stronger affinity for CaO and $Al_2O_3$, leading to a shift in the main minerals in coal ash from silicates to phosphates, which are preferentially separated from silica. He *et al.* [18] examined the sintering behavior of coal ash and phosphorus-rich biomass ash under gasification conditions, and concluded that the formation of Ca-Mg and K-Mg phosphates led to increased sintering temperatures. Shao *et al.* [20] investigated the agglomeration characteristics of sludge combustion in a bench-scale fluidized bed combustor. It has been found that alkali phosphates together with the eutectics of $Fe_2O_3$ and $SiO_2$ significantly influence bed agglomeration during sludge combustion, by forming low-melting point compounds.

SS has a high phosphorus content mainly because flocculants (*e.g.*, Fe-based flocculants) added during sewage treatment capture orthophosphate ions and then cause their precipitation [21,22]. Furthermore, the application of quicklime for dewatering and disinfecting of SS introduces calcium phosphate into the sludge. Therefore, the primary inorganic phosphorus in the sludge includes calcium- and iron-phosphates. According to the above literature review, current research efforts aim to elucidate the mechanisms underlying the influence of phosphorus addition on ash fusion from the perspective of mineral transformation [17,23–26]. During the coal ash melting process, the initial formation of the liquid phase and its characteristics play crucial roles in the subsequent melting behavior of coal ash [27]. Apart from the mineral transformation at high temperatures, the formation of the liquid phase is likely to affect the dissolution of refractory minerals, changing the ash fusion fusibility. However, there is still a lack of direct evidence to confirm that the phosphorus-bearing liquid phase formed during the co-gasification of coal and SS can enhance the dissolution of refractory minerals such as mullite in the coal ash.

In this study, the fusion characteristics of coal ash with the addition of phosphorus were systematically explored. Two types of phosphates were used as phosphorus-bearing additives: calcium phosphate and iron phosphate. To eliminate the effects of calcium and iron on the ash fusion temperature, their respective oxides (CaO and $Fe_2O_3$) were also incorporated for comparison. The mineral composition of the treated ash was determined using X-ray diffraction (XRD), and the modes of occurrences of phosphorus were analyzed using X-ray photoelectron spectroscopy (XPS). Thermal platform microscopy was used to examine the dissolution of mullite in the initial phosphorus-bearing liquid phases formed during ash fusion. The findings of this study are anticipated to offer direct evidence for clarifying the ash fusion mechanism influenced by phosphorus in the ash.

## 2. Experimental

### 2.1. Properties of coal sample

A bituminous coal sample, designated as PXC, obtained from the Huainan Coal Mine in China was prepared for analysis. It underwent drying and subsequent pulverization to achieve a particle size below 100 μm. The proximate analysis, ultimate analysis, and calorific value of the coal sample are presented in Table 1. Proximate analysis on an air-dried basis revealed an ash content of 24.45% and a volatile matter content of 27.54%. Ultimate analysis on a dry basis indicated carbon and hydrogen contents of 62.61% and 3.88%, respectively, with gross calorific value of 25.24 $MJ \cdot kg^{-1}$. Coal ash composition analysis conducted *via* X-ray fluorescence (XRF) spectrometer demonstrated a predominance of silica ($SiO_2$) and alumina ($Al_2O_3$), which collectively constituted 84.08% of the ash matrix (Table 2). The $Fe_2O_3$ and CaO contents of the ash were 4.40% and 6.03%, respectively. The $P_2O_5$ content was 0.13%.

The mineralogical composition of the PXC coal and its ash (prepared at 815 °C in a muffle furnace according to GB/T 212—2008) was characterized using XRD. The results are shown in Fig. 1. The primary minerals identified in the raw coal were quartz ($SiO_2$), kaolinite ($Al_2Si_2O_5(OH)_4$), calcite ($CaCO_3$), and ferroan

**Table 1**
Proximate analysis, ultimate analysis, and calorific value of the raw coal sample.

| Proximate analysis/% | | | | Ultimate analysis/% | | | | | Calorific Value/$MJ \cdot kg^{-1}$ |
|---|---|---|---|---|---|---|---|---|---|
| $M_{ad}$ | $A_{ad}$ | $V_{ad}$ | $FC_{ad}$ | $C_d$ | $H_d$ | $O_d$ | $N_d$ | $S_{t,d}$ | $Q_{gr,d}$ |
| 1.54 | 24.45 | 27.54 | 46.47 | 62.61 | 3.88 | 7.18 | 1.12 | 0.38 | 25.24 |

**Table 2**
Chemical composition of the coal ash (%).

| $Al_2O_3$ | $SiO_2$ | $Fe_2O_3$ | CaO | MgO | $K_2O$ | $Na_2O$ | $P_2O_5$ | $SO_3$ |
|---|---|---|---|---|---|---|---|---|
| 32.67 | 51.41 | 4.40 | 6.03 | 0.78 | 0.79 | 0.67 | 0.13 | 1.67 |

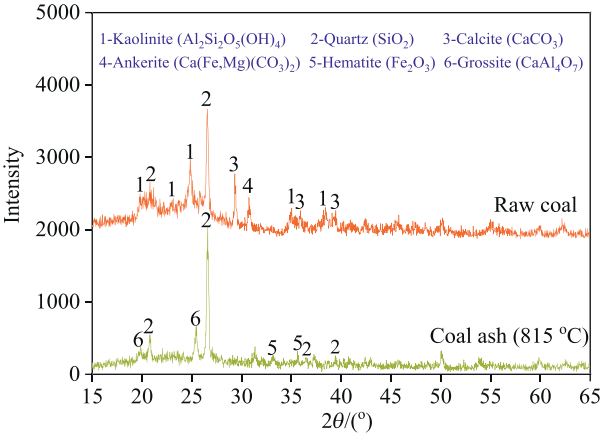


**Fig. 1.** XRD patterns of the raw coal and ash.

dolomite ($Ca(Fe,Mg)(CO_3)_2$). Following ashing treatment, the resultant ash products exhibited distinct phase transformations, with quartz ($SiO_2$), grossite ($CaAl_4O_7$), and trace hematite ($Fe_2O_3$) being detected as the dominant crystalline phases, which are consistent with the chemical composition of the ash presented in Table 2.

### 2.2. Experimental procedures

To investigate the effect of phosphorus on the melting temperature of coal ash, four additives calcium phosphate ($Ca_3(PO_4)_2$, analytical reagent-grade purity), iron phosphate ($FePO_4 \cdot 4H_2O$, analytical reagent-grade purity), calcium oxide (CaO, analytical reagent-grade purity), and iron oxide ($Fe_2O_3$, analytical reagent-grade purity) were individually mixed with the coal. The $Ca_3(PO_4)_2$ and $FePO_4 \cdot 4H_2O$ additives were blended into the coal at concentrations of 2%, 4%, 6%, 8%, and 10% by mass, with the resulting samples labeled as CaP2-CaP10 and FeP2-FeP10, respectively. Because calcium and iron significantly affect the ash fusion temperature, CaO and $Fe_2O_3$ were also added to the coal in amounts equivalent to the calcium and iron contents present in the corresponding phosphates. These samples were designated Ca2–Ca10 and Fe2–Fe10, respectively. The concentrations of the all four additives are presented in Table 3.

Coal samples mixed with additives of varying concentrations were combusted in a muffle furnace at 815 °C. The ash fusion characteristic temperatures, including the deformation temperature (DT), softening temperature (ST), hemisphere temperature (HT), and flow temperature (FT) were measured using an ash melting point analyzer (5E-AF3000, Changsha Kaiyuan, China) under a weakly reducing atmosphere, with a maximum operational temperature limit of 1500 °C. The samples were heated from room temperature to 1000 °C at 10 °C·min$^{-1}$ and 1000–1500 °C at 5 °C·min$^{-1}$. To investigate the mineral phase transformations induced by different additives at elevated temperatures, ash samples were heat-treated in an electric furnace at temperatures ranging from 1100°C to 1400 °C within a controlled atmosphere of 60% CO and 40% $CO_2$. After 20 min of thermal treatment, the resulting ash/slag was rapidly removed from the furnace, quenched in deionized water, dried, pulverized, and then subjected to XRD analysis.

### 2.3. Sample characterizations

The mineral composition of the ash/slag samples was characterized using XRD (XD-3 model, PERSEE, China) with Cu-$K_\alpha$-radiation. The diffractometer was operated at 36 kV and 40 mA, with a scan rate of 2(°)·min$^{-1}$. Phase identification was performed using Jade software (version 5.0) to analyze the obtained diffraction patterns. A chemical composition analysis was conducted using XRF (3600 model, Thermo Fisher, USA). Phosphorus speciation in the ash/slag was investigated using XPS (ESCALAB Xi+, Thermo Scientific) with an Al $K_\alpha$ excitation source focused on the P 2p orbital. All binding energies were calibrated against the C 1s peak at 284.0 eV.

The ash melting behavior was observed *in situ* using a thermal platform microscope system. The system comprised of a thermal platform (TS1500, Linkam, Britain), a water-cooling system, a microscope (DM 2700 P, Leica, Germany), a gas system, and an image acquisition system. Approximately 2 mg of ash sample was loaded into an alumina crucible and heated from the ambient temperature to 1400 °C under a nitrogen atmosphere. The thermal program involved two stages: rapid heating at 80 °C·min$^{-1}$ up to 1000 °C followed by a slower ramp of 20 °C·min$^{-1}$ to the target temperature. Real-time morphological changes during heating were continuously recorded, and a quantitative analysis of the cross-sectional area with respect to the temperature was performed using Image J software.

**Table 3**
Contents of the four additives added to the coal sample.

| Sample | Composition | Sample | Composition |
|---|---|---|---|
| CaP2 | PXC+2.00%$Ca_3(PO_4)_2$ | Ca2 | PXC+1.09%CaO |
| CaP4 | PXC+4.00%$Ca_3(PO_4)_2$ | Ca4 | PXC+2.17%CaO |
| CaP6 | PXC+6.00%$Ca_3(PO_4)_2$ | Ca6 | PXC+3.25%CaO |
| CaP8 | PXC+8.00%$Ca_3(PO_4)_2$ | Ca8 | PXC+4.34%CaO |
| CaP10 | PXC+10.00%$Ca_3(PO_4)_2$ | Ca10 | PXC+5.42%CaO |
| FeP2 | PXC+2.00%$FePO_4 \cdot 4H_2O$ | Fe2 | PXC+0.72%$Fe_2O_3$ |
| FeP4 | PXC+4.00%$FePO_4 \cdot 4H_2O$ | Fe4 | PXC+1.43%$Fe_2O_3$ |
| FeP6 | PXC+6.00%$FePO_4 \cdot 4H_2O$ | Fe6 | PXC+2.15%$Fe_2O_3$ |
| FeP8 | PXC+8.00%$FePO_4 \cdot 4H_2O$ | Fe8 | PXC+2.87%$Fe_2O_3$ |
| FeP10 | PXC+10.00%$FePO_4 \cdot 4H_2O$ | Fe10 | PXC+3.58%$Fe_2O_3$ |

### 2.4. Thermodynamic equilibrium calculation

The mineral composition of coal ash at different temperatures was predicted using the thermodynamic equilibrium calculation software FactSage 8.1. The calculation input conditions were based on a 100 g ash sample, and the amount of each component was calculated according to the ash chemical compositions presented in Table 2. The reactant gas used for simulating a weakly reducing atmosphere was a mixture of CO and $N_2$ at a volume ratio of 2:3. The temperature range for the calculations was 1000–1500 °C, with intervals of 50 °C. FactPs and Ftoxid were used for the calculations. Formation of the liquid phase was predicted using the FToxid-SLAGA and FToxide-Mull modules.

## 3. Results and Discussion

### 3.1. Effects of phosphorus on ash fusion temperatures

Because the ash FT is a crucial indicator for evaluating slag fluidity and determining the operating temperature of gasifiers, calcium and iron -phosphates were mixed with coal to investigate their effects on the ash FT. To exclude the effects of Ca and Fe on the FT, CaO and $Fe_2O_3$ were also added for comparison. The quantities of CaO and $Fe_2O_3$ added were equal to those in $Ca_3(PO_4)_2$ and $FePO_4 \cdot 4H_2O$, respectively. Fig. 2 illustrates the variation in the coal ash fusion temperatures with different additive contents. Regardless of whether the compounds contained Ca or Fe, the FT decreased as the additive content increased. For instance, the addition of 10% $Ca_3(PO_4)_2$ reduced the FT of the ash from above 1500°C to 1348 °C (Fig. 2(a)), while the addition of 10% $FePO_4 \cdot 4H_2O$ caused the FT decrease from above 1500°C to 1252 °C (Fig. 2(c)). Comparing the effects of $Ca_3(PO_4)_2$ and CaO in Fig. 2(a) and (b), respectively, revealed that the decrease in the FT with $Ca_3(PO_4)_2$ exceeded that with the addition of CaO. Similar results were observed with the addition of $FePO_4 \cdot 4H_2O$ and $Fe_2O_3$, shown in Fig. 2(c) and (d). These findings indicate that in addition to Ca and Fe, phosphorus reduced ash FT.

To evaluate the effect of phosphorus on reducing the ash FT, $\Delta T$, which was defined as the difference in FT between the phosphate additives and the corresponding oxide addition, was calculated. The relationship between $\Delta T$ and the additive ratio is illustrated in Fig. 2(e). As the additive content increased, $\Delta T$ increased consistently for both Ca- and Fe-bearing additives. Notably, the $\Delta T$ for the $Fe_2O_3$-$FePO_4 \cdot 4H_2O$ system (denoted as Fe-FeP) exceeded that for the CaO-$Ca_3(PO_4)_2$ system, although the phosphorus content in $FePO_4 \cdot 4H_2O$ is 16.5%, which is lower than that in $Ca_3(PO_4)_2$ (20%). This observation suggests that Ca and Fe not only independently

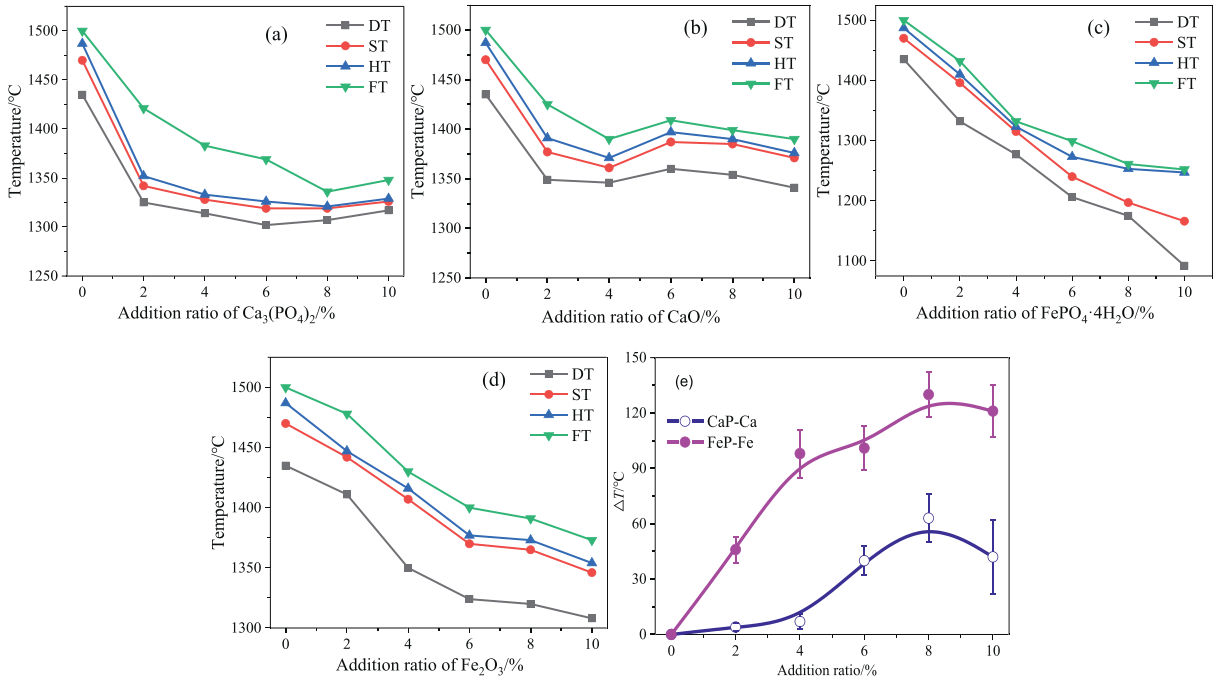


**Fig. 2.** Fusion temperatures of the ash with respect to the added ratio of calcium/iron-phosphate and the corresponding oxides.

reduce the ash FT, but also modulate the effectiveness phosphorus in reducing the FT. The $Al_2O_3/(CaO + Na_2O + K_2O)$ (A/CNK) ratio decreases with increasing $Ca_3(PO_4)_2$ content. In this case, Ca preferentially reacted with phosphorus and iron to form refractory minerals such as calcium iron phosphate ($Ca_9Fe(PO_4)_7$) [14], which diminished phosphorus's impact on the ash FT. In contrast, the addition of $FePO_4·4H_2O$ caused minimal changes to the A/CNK ratio, maximizing phosphorus's ability to reduce the ash FT.

### 3.2. Dependence of mineral transformation on phosphorus addition

Mineral transformation is a critical factor influencing the ash FT [28–30]. To investigate the role of phosphorus in modifying the mineral composition of coal ash, the coal was blended with $Ca_3(PO_4)_2$, $FePO_4·4H_2O$, and the corresponding oxides at contents of 4% and 8%, respectively. The mixed coal samples were combusted in a muffle furnace at 815 °C, and the resulting ashes were subsequently heated to 1100, 1200, 1300, and 1400 °C, respectively. XRD analysis was conducted to identify the crystalline minerals. Fig. 3 shows the XRD patterns of the PXC ash without additives. At 815 °C, the dominant minerals detected in the ash were quartz ($SiO_2$) and grossite ($CaAl_4O_7$). With increasing temperature, the primary minerals gradually transformed into anorthite ($CaAl_2Si_2O_8$) and mullite ($Al_6Si_2O_{13}$). Substantially, mullite emerged as the sole crystalline mineral in the ash after treatment at 1400 °C.

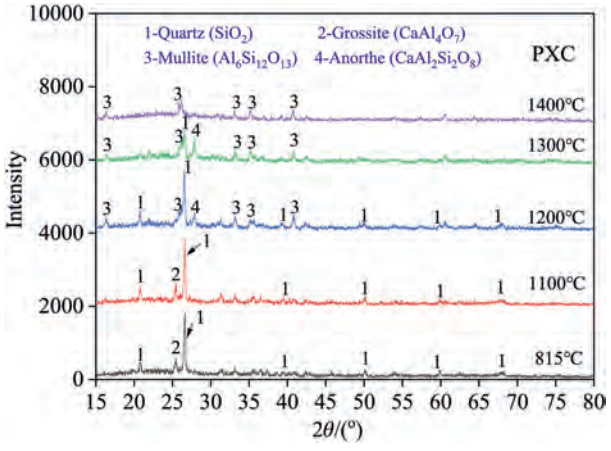


**Fig. 3.** XRD patterns of the PXC ash treated at different temperatures.

The XRD patterns of the Ca4, Ca8, CaP4, and CaP8 ash samples at different temperatures are shown in Fig. 4. Regardless of the CaO content, the dominant mineral phases observed at 815 °C were quartz, gehlenite ($Ca_2Al_2SiO_7$), grossite, and lime (CaO). With increasing temperature, the diffraction peak intensities corresponding to anorthite ($CaAl_2Si_2O_8$) increased, reaching maximum values at 1300 °C. Concurrently, the peak intensities for quartz, grossite, and lime decreased, as shown in Fig. 4(a) and (b). This trend indicated that the formation of anorthite occurred through chemical reactions among quartz, lime, and grossite, as expressed by reaction (1). This process was thermodynamically favorable, as evidenced by negative $\Delta G$ values at both 1100 and 1300 °C. Remarkably, anorthite persisted in the treated ash even at 1400 °C.

$$4SiO_2 + CaO + CaAl_4O_7 \rightarrow 2CaAl_2Si_2O_8$$

$$(\Delta G_{1100} = -24.72\ \text{kJ} \quad \Delta G_{1300} = -28.29\ \text{kJ}) \tag{1}$$

The primary mineral phases identified in the CaP4 and CaP8 ashes at 815 °C were quartz, berlinite ($AlPO_4$), hydroxyapatite ($Ca_5(PO_4)_3(OH)$), and grossite, as shown in Fig. 4(c) and (d). When the temperature ranged from 1100 to 1400 °C, anorthite crystallized, with its diffraction peak intensity reaching maximum values at 1300 °C. Concurrently, the characteristic peaks of quartz and berlinite exhibited progressive attenuation. The formation of berlinite and the eutectic between $AlPO_4$ and $SiO_2$ reduces the ash fusion temperatures by preventing the transformation of $Al_2O_3$ into refractory aluminosilicates and corundum [15]. Notably,

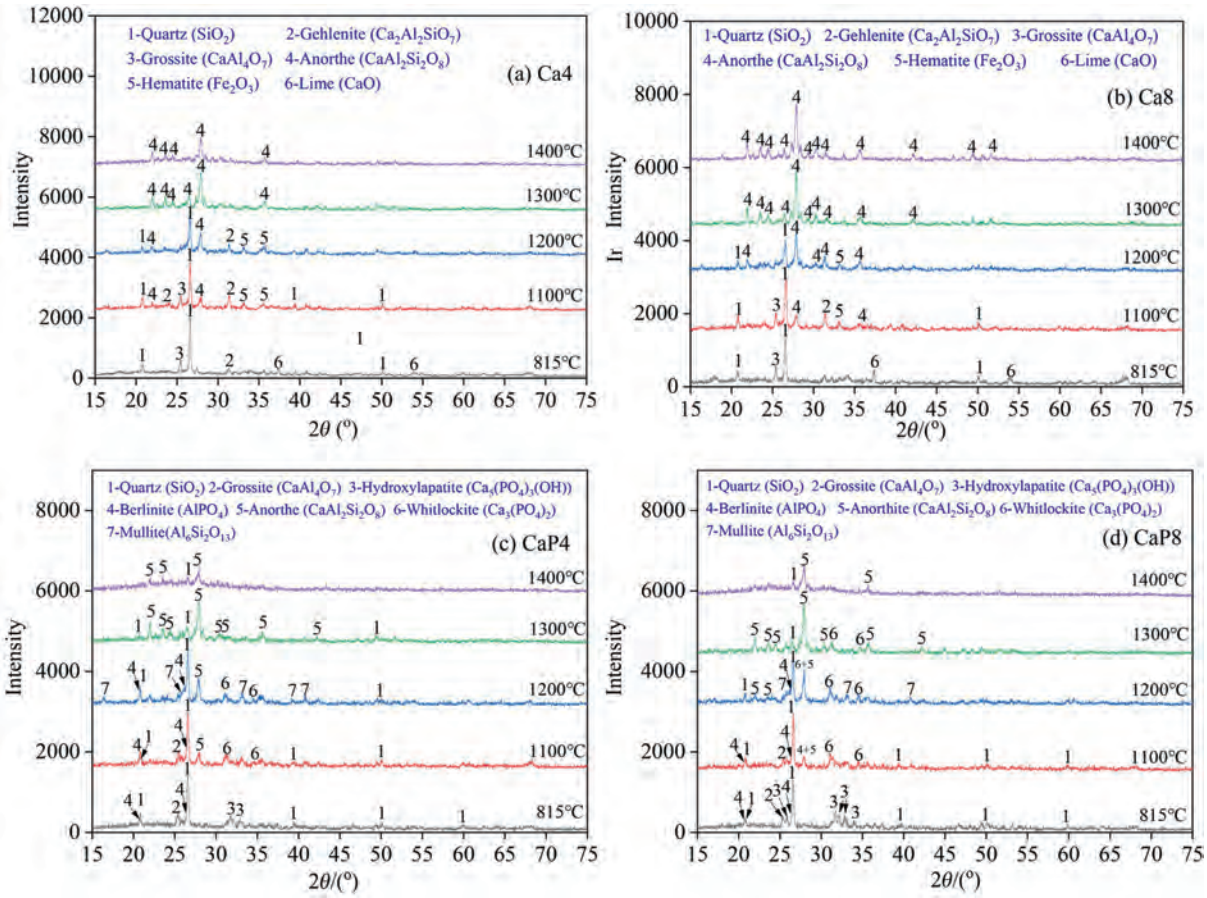


**Fig. 4.** XRD patterns of Ca4, Ca8, CaP4 and CaP8 treated at different temperatures.

whitlockite ($Ca_3(PO_4)_2$) emerged in CaP4 ashes within the range of 1100–1200 °C, whereas it persisted up to 1300 °C in CaP8 ashes. Upon further heating to 1400 °C, trace amounts of anorthite and quartz remained detectable in both systems, although their peak intensities were significantly diminished compared with those observed in the Ca4 and Ca8 references, respectively. This intensity reduction suggests that the ash FT of $Ca_3(PO_4)_2$ was intrinsically lower than that of the CaO additives when compared with equivalent calcium content levels.

Fig. 5 shows the XRD patterns of the Fe4, Fe8, FeP4, and FeP8 samples subjected to different treatment temperatures. As shown in Fig. 5(a) and (b), the ash of Fe4 and Fe8 at 815 °C primarily consisted of quartz, grossite, and hematite ($Fe_2O_3$). When the temperature was increased to 1100 °C, mullite formation occurred, and its diffraction peak intensity gradually decreased as the temperature increased to 1400 °C. In the case of FeP4 (Fig. 5(c)), the dominant minerals at 815 °C were quartz, grossite, aluminum phosphate and hematite. These phases exhibited reduced peak intensities with increasing temperature. At 1100 °C, mullite and anorthite emerged, although their peak intensities decreased with the increasing temperature. Complete disappearance of mineral diffraction peaks at 1400 °C indicated an essentially molten ash state. A distinct contrast was observed for FeP8 (Fig. 5(d)), where only quartz persisted in the ash at 1200 °C. No crystalline mineral peaks were present for FeP8 above 1300 °C, whereas mullite remained present in Fe8 at 1400 °C. This indicates that FeP8 achieved full melting of the ash at lower temperatures than Fe8. Generally, the iron in coal ash slag at high temperatures is preferentially associated with aluminosilicate to form ferrosilicate, hercynite and/or fayalite [31,32]. However, according to the XRD results, hematite was the sole Fe-bearing crystalline mineral in this study. The hematite in the slag likely formed a solid solution with other minerals and maintained similar structure according to the research results on the crystal composition of iron-rich coal slag during continuous cooling [33]. The co-existence of aluminum phosphate, quartz, and hematite in the FeP4 and FeP8 samples readily formed a low-temperature eutectic, which reduced the ash fusion temperatures.

### 3.3. Mechanisms of ash fusion temperature affected by phosphorus addition

To further investigate the mechanism whereby the addition of phosphorus affects the ash fusion temperature, the vaporization ratio of phosphorus during thermal treatment was calculated according to Eq. (2)

$$\text{Vaporization ratio of P} = \frac{m_1 - m_2}{m_1} \times 100\% \quad (2)$$

where $m_1$ and $m_2$ represent the mass of phosphorus in the ash before and after thermal treatment, respectively. The vaporization ratios of phosphorus in CaP4, CaP8, FeP4, and FeP8 as a function of temperature are shown in Fig. 6. Fig. 6(a) and (b) present the experimental results for phosphorus vaporization. The vaporization ratio of phosphorus increased with the temperature, regardless of the addition of calcium or iron-phosphate. Notably, the phosphorus vaporization ratio was higher for CaP8 and FeP8

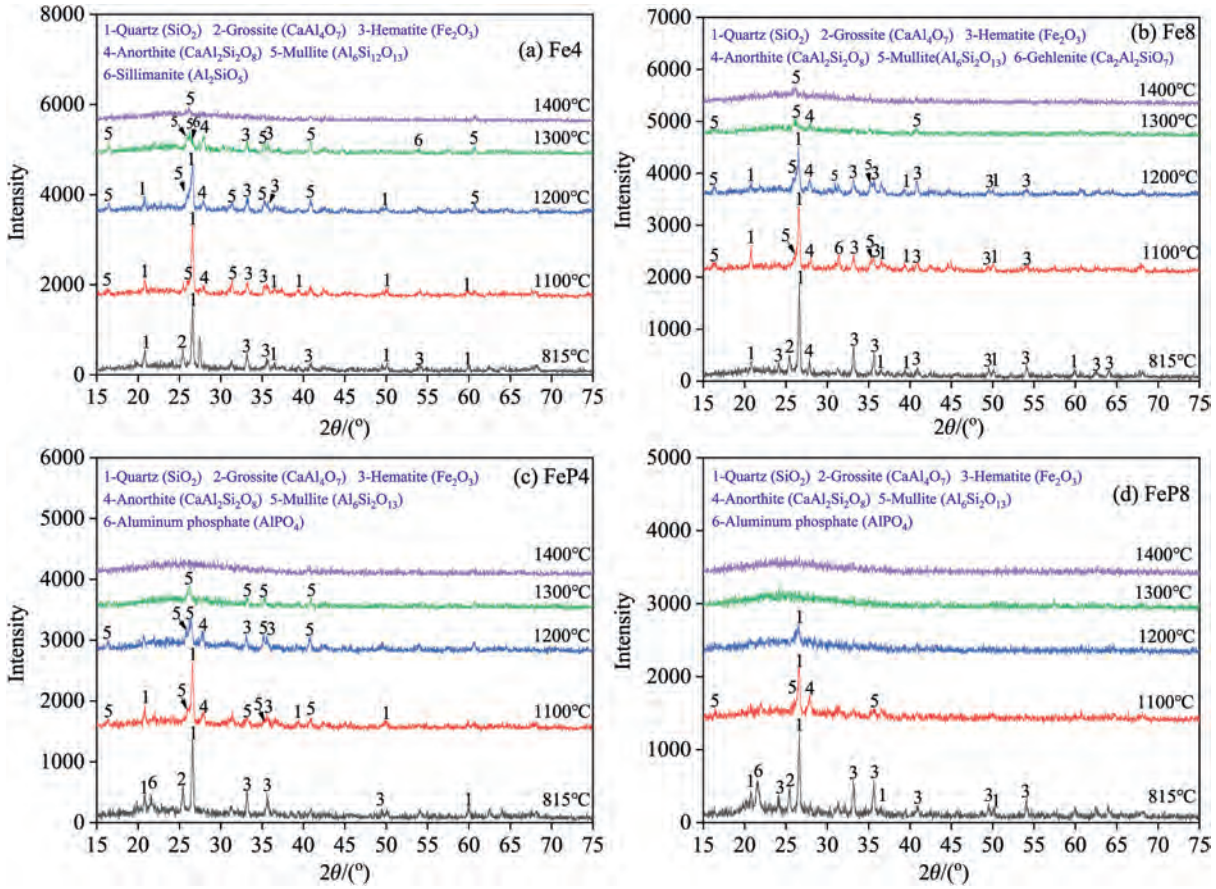


**Fig. 5.** XRD patterns of Fe4, Fe8, FeP4, and FeP8 treated at different temperatures.

than for CaP4 and FeP4. Additionally, the ash containing iron phosphate exhibited a higher phosphorus vaporization ratio than that with calcium phosphate, suggesting that FeP has a stronger propensity for phosphorus volatilization than CaP at temperatures below 1300 °C. This difference is attributed to the lower melting point of $FePO_4$ (1000 °C) relative to $Ca_5(PO_4)_3$ (1670 °C). However, when the temperature exceeded 1300 °C, the vaporization ratios of phosphorus in CaP8 and FeP8 became comparable, with approximately 50% of phosphorus retained in both slags.

Apart from the experimental observations, phosphorus vaporization behavior was predicted *via* thermodynamic equilibrium calculations using FactSage 8.1. The results are shown in Fig. 6(c) and (d). As the temperature increased, the vaporization rate of phosphorus in the CaP4 sample increased and then decreased, whereas that of phosphorus in the CaP8 sample simply increased. The declining trend of phosphorus vaporization at >1150 °C in the CaP4 sample was caused by dissolution of phosphorus in the liquid phase, as shown in Fig. 6(c). In the FeP4 and FeP8 samples, the volatility of phosphorus exhibited an increasing trend (Fig. 6(d)). Compared with the experimental results, the predicted vaporization ratio of phosphorus was higher under identical conditions, which is attributed to the kinetic limit of phosphorus vaporization during heating.

The phosphorus speciation in the ash was characterized using XPS. Fig. 7 presents high-resolution XPS scans of treated ash with CaP8 and FeP8 additives at 1200 and 1400 °C, revealing two distinct phosphorus-bearing species: $P_2O_5$ and $PO_4^{3-}$. Quantitative analysis through spectral deconvolution demonstrated that $P_2O_5$ corresponds to phosphorus dissolved in the molten slag, while $PO_4^{3-}$ represents phosphorus incorporated into crystalline phosphate phases. In the case of CaP8 at 1200 °C, the $P_2O_5$ content was determined to be 24.2%, which significantly increased to 51.2% when the temperature was elevated to 1400 °C, as shown in Fig. 7 (a) and (b). This temperature-dependent enhancement improved the phosphorus dissolution in the molten slag. A similar trend was observed for FeP8 (Fig. 7(c) and (d)). Notably, the FeP8 sample at 1400 °C exhibited a substantially higher $P_2O_5$ content of 71.4% (Fig. 7(d)) than CaP8 (51.2%) under identical conditions (Fig. 7(b)). This result suggests that Fe promotes the dissolution of phosphorus into the molten slag compared with Ca, potentially contributing to a decrease in the ash fusion temperature.

Thermodynamic equilibrium calculations were conducted to further investigate the mineral transformations and liquid phase formation during heating with additives. The calculation results for PXC ash without additives are presented in Fig. 8. The primary minerals in the ash at 1000 °C included mullite, quartz, anorthite, ferrocordierite ($Fe_2Al_4Si_5O_{18}$), and magnesium cordierite ($Mg_2Al_4Si_5O_{18}$). As the temperature increases, the liquid phase fraction gradually increases. Quartz and magnesium cordierite melted at 1250 °C, while anorthite disappeared at 1350 °C. By 1500 °C, approximately 15% of mullite remained, resulting in the FT of PXC ash exceeding 1500 °C, as shown in Fig. 2.

The calculation results for mineral transformation at temperatures ranging from 1000°C to 1500 °C with the addition of CaO and $Ca_3(PO_4)_2$ are presented in Fig. 9. Fig. 9(a) shows the fraction of the liquid phase formed as a function of temperature. Typically, the temperature at which 90% of the liquid phase was formed was considered to be close to the FT of ash [34]. Based on the calculation results, the temperatures required for 90% liquid formation under the conditions of CaP4 and CaP8 were lower than those

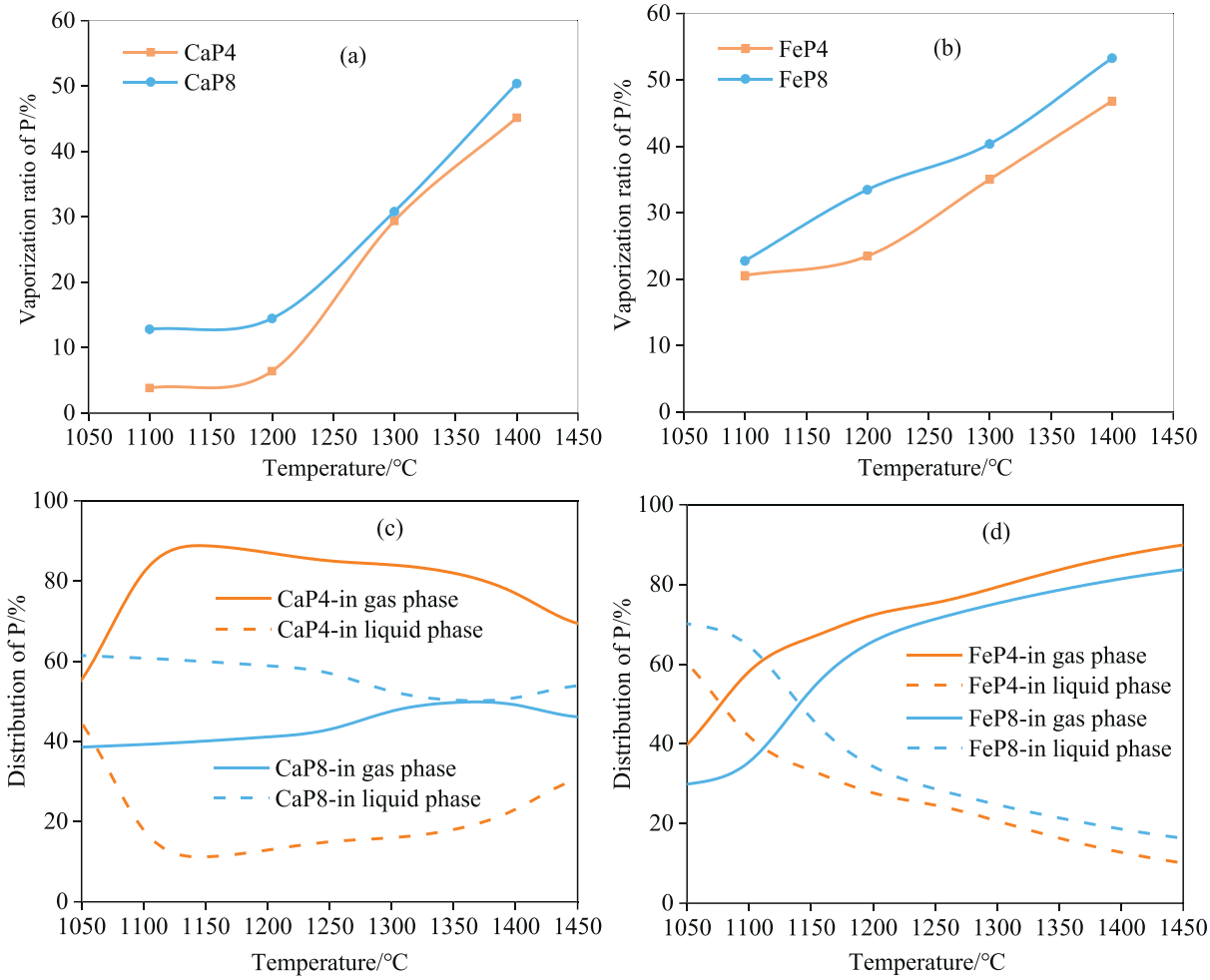


**Fig. 6.** Vaporization ratio of phosphorus with respect to temperature: (a, b) experimental results; (c, d) predicted results.

under the Ca4 and Ca8 conditions. This indicates that the addition of calcium phosphate is more effective for reducing the FT than the addition of CaO. Additionally, the temperatures corresponding to 90% liquid phase formation under the Ca4 and Ca8 conditions were almost identical, indicating comparable FTs for ash under these two conditions. This is consistent with the experimental results for the ash FT shown in Fig. 2(b).

With regard to the mineral transformations, the major crystalline minerals at 1000 °C in the case of Ca4 were anorthite and Fe-/Mg-cordierite, as shown in Fig. 9(b). The total fraction exceeded 80%. As the temperature increased, cordierite was completely melted at 1250 °C, while anorthite disappeared at 1500 °C. In Ca8 ash, the dominant minerals at 1000 °C included anorthite, wollastonite ($CaSiO_3$), and a small amount of diopside ($CaMgSi_2O_6$) (Fig. 9(c)). The fraction of the liquid slag phase reached 100% at 1500 °C, which was similar to that of Ca4. In the case of CaP4, the primary minerals at 1000 °C were quartz, mullite, and anorthite, as shown in Fig. 9(d). The total fraction of minerals decreased with increasing temperature. Similar results were obtained for CaP8 (Fig. 9(e)). In contrast, a small amount of potassium feldspar ($KAlSi_3O_8$) was formed in CaP8, which was not observed in CaP4.

The thermodynamic calculation results for mineral transformation and liquid phase formation in the Fe4, Fe8, FeP4, and FeP8 samples at different temperatures are shown in Fig. 10. The temperature required to achieve 90% liquid phase formation in FeP8 was the lowest among all the samples (Fig. 10(a)), which is consistent with the experimental results shown in Fig. 2(c). Regarding mineral transformation, the primary minerals in the Fe4 sample were mullite, anorthite, and Fe-/Mg-cordierite, and the total fraction of these minerals decreased as the temperature increased (Fig. 10(b)). The mineral composition of Fe8 sample (Fig. 10(c)) was the same as that of Fe4 sample. In the case of FeP4, mullite, quartz, anorthite, and Fe-cordierite were the dominant minerals in the ash at 1000 °C (Fig. 10(d)). At this temperature, the fraction of liquid slag was approximately 25%, which was higher than that of Fe4. This suggests that the addition of FeP4 promoted the formation of liquid slag and facilitated ash fusion. When the iron phosphate content increased from 4% to 8%, anorthite disappeared, and a small amount of potassium feldspar was formed at 1000 °C (Fig. 10(e)). Furthermore, the fraction of liquid slag increased from 25% in FeP4% to 30% in FeP8 at 1000 °C, indicating that the liquid slag formation was more likely to occur in the FeP8 sample.

### *3.4. Melting process of ash with calcium/iron phosphate and their oxides*

The melting processes of the Ca8, CaP8, Fe8, and FeP8 samples were observed using a thermal platform microscope. The morphologies of the ash at 1000–1400 °C are illustrated in Fig. 11.

To evaluate the ash melting process quantitatively, the rate of change of the cross-sectional area of each sample as a function of temperature was calculated according to Eq. (3).

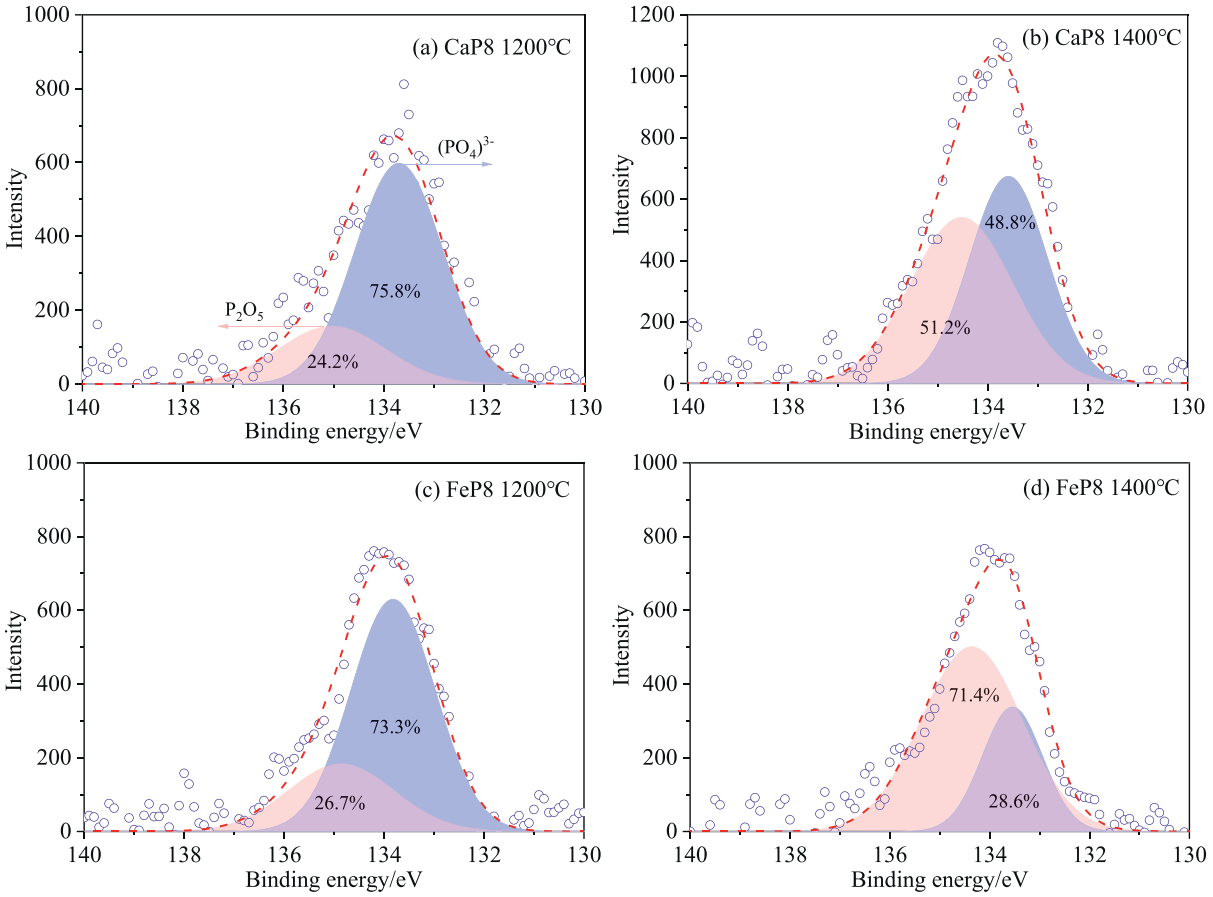


**Fig. 7.** XPS spectra of phosphorus (P 2p) in the treated ash with CaP8 and FeP8 addition at 1200 and 1400 °C.

$$\Delta A = \frac{A_T - A_{1000}}{A_{1000}} \times 100\% \quad (3)$$

where, $\Delta A$ denotes the rate of change of the cross-sectional area, and $A_T$ and $A_{1000}$ represent the cross-sectional areas of the ash at temperature $T$ and 1000 °C, respectively. These areas were determined using Image J software.

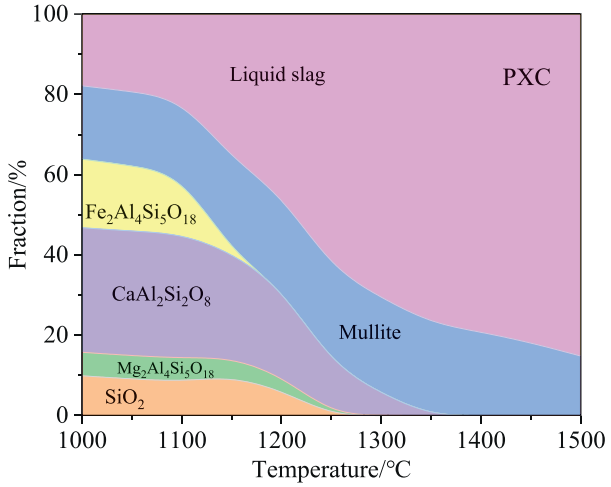


**Fig. 8.** Thermodynamic calculation results for the mineral transformation of PXC ash at different temperatures.

The temperature-dependent variations in $\Delta A$ for the ash samples are shown in Fig. 12. As illustrated in Fig. 12(a), the $\Delta A$ values for both samples initially decreased and then increased, reflecting sequential stages of shrinkage, fusion, and expansion during the ash melting process. Both Ca8 and CaP8 samples exhibited initial shrinkage at 1050 °C, which is attributed to liquid phase formation. Notably, CaP8 demonstrated a higher shrinkage rate than Ca8 at temperatures below 1250 °C, suggesting enhanced liquid phase generation in the phosphorus-containing ash. The minimum $\Delta A$ values occurred at 1250 °C for CaP8 and 1350 °C for Ca8, respectively. Beyond these critical temperatures (1250 °C for CaP8 and 1350 °C for Ca8), accelerated mineral melting and dissolution processes were observed. This thermal behavior was more pronounced in the Fe-containing samples (Fe8 and FeP8), as shown in Fig. 12(b). In the case of FeP8, the maximum shrinkage was observed at 1100 °C, a lower temperature compared with CaP8 (1250 °C), indicating that the addition of FeP8 was more beneficial to the ash melting.

### 3.5. Dissolution behavior of mullite in P-containing liquid phase

The ash fusion behavior is ascribed to two mechanisms: softening-melting and melting-dissolution [27,35]. The softening-melting mechanism is related to the formation of minerals with low melting point, while the melting-dissolution mechanism refers to the formation of an active liquid phase in the initial stage of coal ash, which has a good dissolving capacity for refractory minerals such as mullite. The melting point of mullite is approximately 1870 °C, and its presence affects the ash melting behavior.

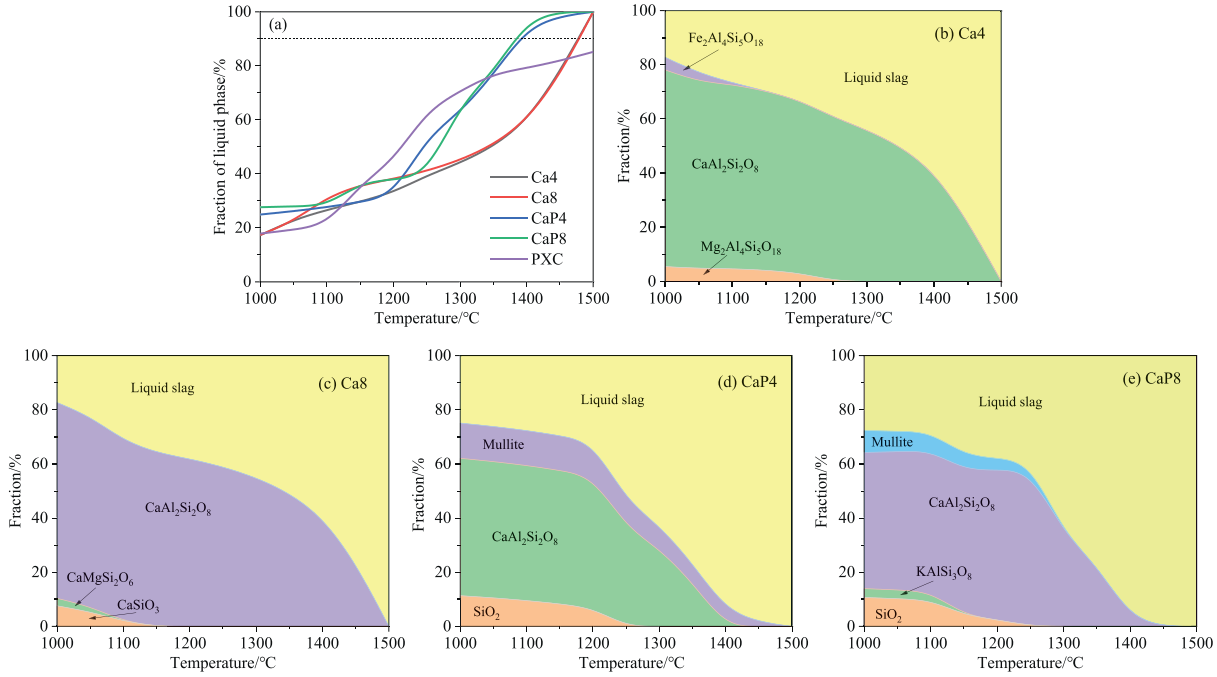


**Fig. 9.** Thermodynamic calculation results for mineral transformation in the cases of Ca4, Ca8, CaP4, and CaP8 addition at different temperatures.

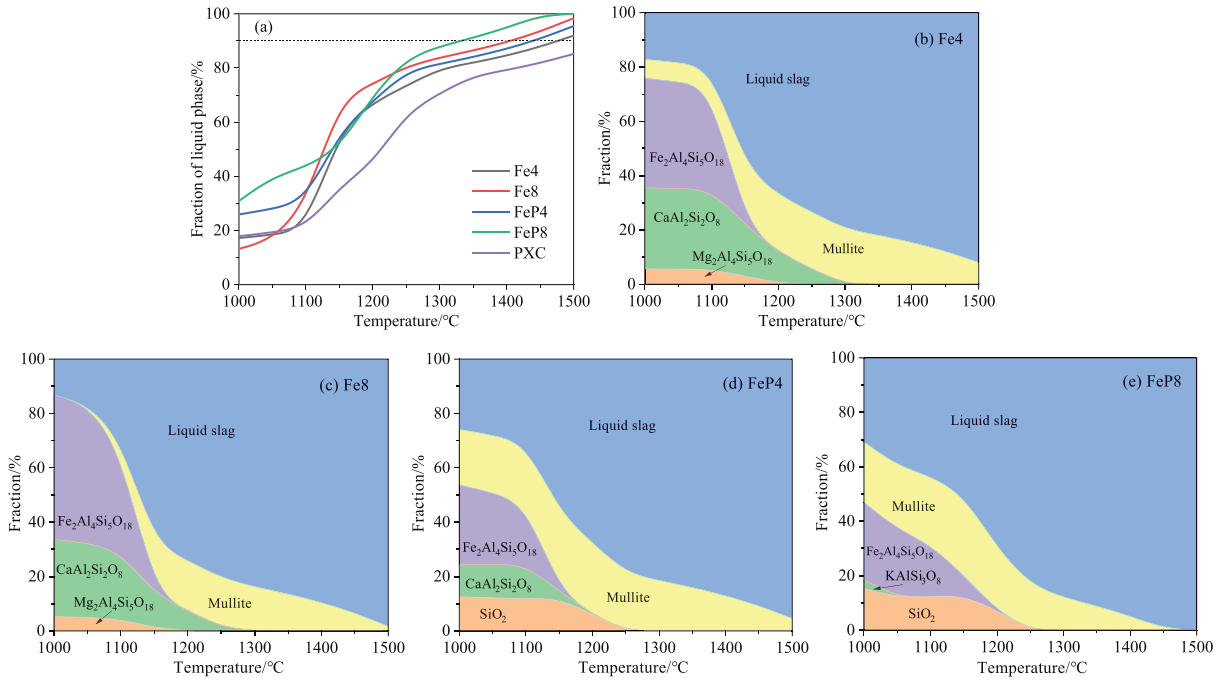


**Fig. 10.** Thermodynamic calculation results of mineral transformation in the case of Fe4, Fe8, FeP4 and FeP8 at different temperatures.

According to the XRD analysis shown in Figs. 4 and 5, besides the formation of $AlPO_4$, no new P-bearing compounds are detected. Therefore, according to the XRD analysis and thermodynamic equilibrium calculations shown in Figs. 9 and 10, the softening-melting mechanism does not affect the ash fusion temperature. The melting-dissolution mechanism is likely to govern the ash melting behavior with the addition of calcium/iron phosphates.

To confirm this assumption, the dissolution of mullite in phosphorus-containing liquids was investigated using a thermal platform microscope. Ash samples from Ca8, CaP8, Fe8, and FeP8

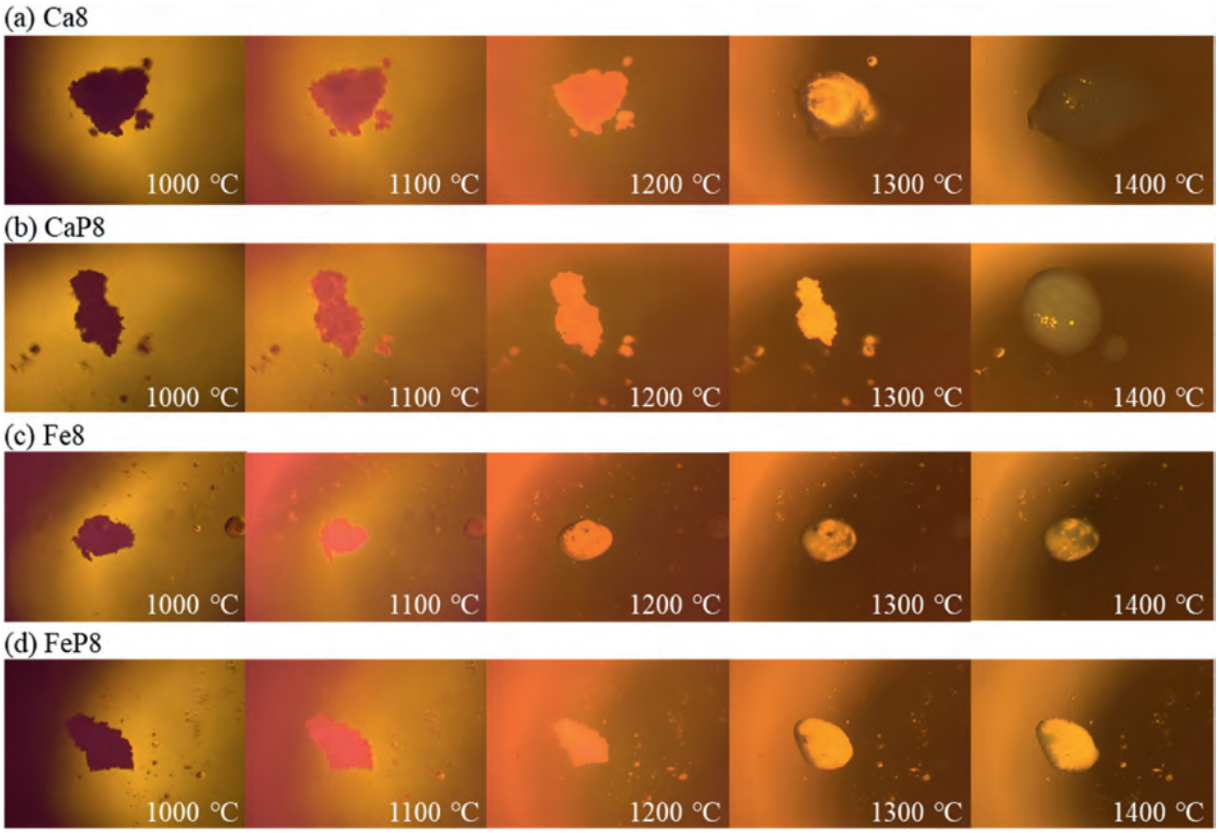


**Fig. 11.** Morphologies of the Ca8, CaP8, Fe8, and FeP8 ash samples at 1000–1400 °C.

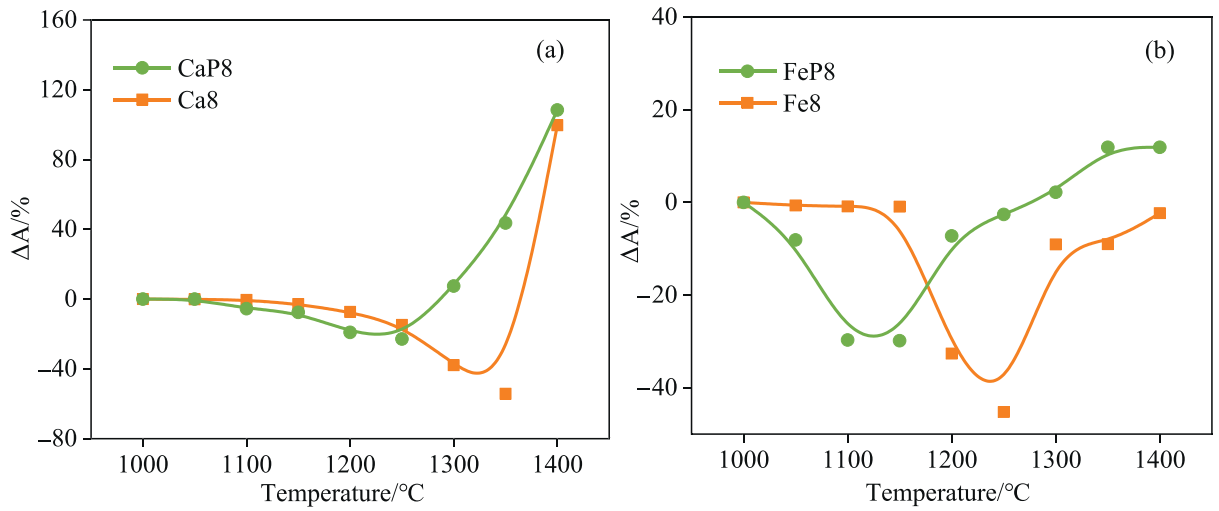


**Fig. 12.** Δ *A* values of the ash samples as a function of temperature.

were spread on corundum plates with mullite particles on their surfaces. Sequential images of mullite dissolution in the Ca8, CaP8, Fe8, and FeP8 ash during heating are shown in Fig. 13. In these micrographs, the white mullite particles contrast the grey/black background of the ash containing different additives. During heating, the ashes underwent preferential melting to form a phosphorus-enriched liquid phase because their fusion temperature was substantially lower than that of mullite. The dissolution behavior of the mullite particles in this phosphorus-containing liquid phase was recorded.

To quantify the dissolution of mullite in the liquid phase, the relative change in the cross-sectional area of the mullite particles was calculated according to Eq. (4).

$$\Delta M = \frac{M_T}{M_{1000}} \times 100\% \tag{4}$$

Where, $\Delta M$ represents the rate of change of the mullite particle cross-sectional area, and $M_T$ and $M_{1000}$ denote the mullite particle cross-sectional areas at temperature $T$ and 1000 °C, respectively.

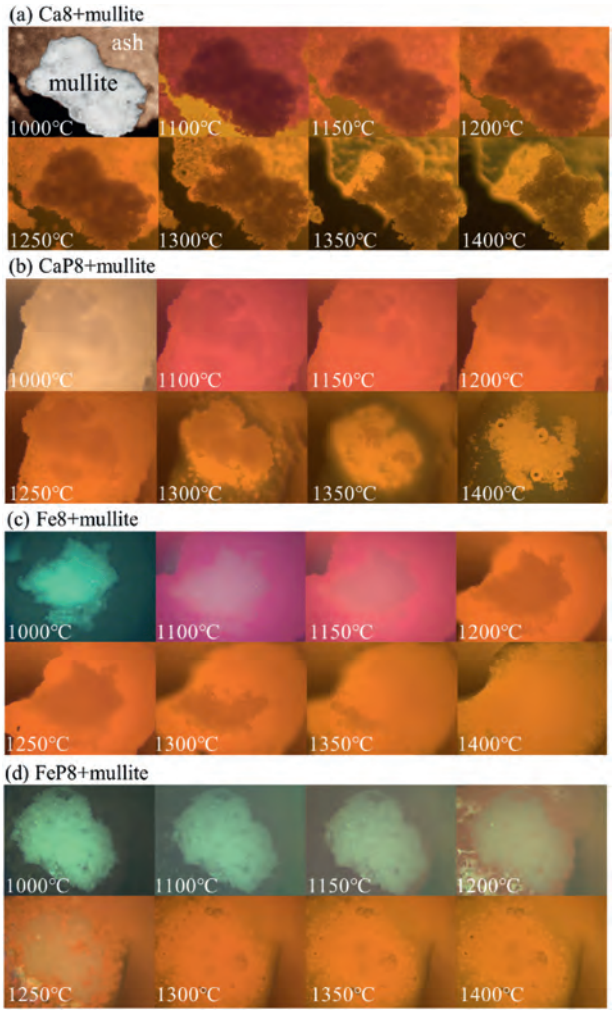


**Fig. 13.** Dissolution of mullite particles in the ash with the addition of Ca8, CaP8, Fe8, and FeP8.

The temperature-dependent variation of $\Delta M$ for mullite under different conditions is depicted in Fig. 14.

Regardless of the additive type, $\Delta M$ exhibited a slight decrease during the initial fusion stage, followed by a rapid decline at elevated temperatures. For instance, in the case of CaP8, $\Delta M$ decreased from 100% at 1000 °C to 91.8% at 1200 °C and further dropped to 0% (indicating complete melting) at 1400 °C (Fig. 14(a)). In contrast, $\Delta M$ was 61.9% at 1400 °C in the case of Ca8. This suggests that the liquid phase in CaP8 has a stronger capacity for dissolving mullite compared with Ca8. Similar results were observed for Fe8 and FeP8, as shown in Fig. 14(b). The dissolving ratio of mullite particles in FeP8 liquids was higher than that in Fe8, as the mullite in FeP8 was completely molten at 1300 °C, while the corresponding temperature was 1400 °C in Fe8. Moreover, the dissolving ability of the liquid phase from FeP8 for mullite particles was superior to that of the liquid phase from CaP8. This was evidenced by the fact that $\Delta M$ was 0% at 1400 °C for CaP8 but at 1300 °C for FeP8, indicating that FeP8 was more effective in reducing the ash FT than CaP8. Combining this observation with the XPS results shown in Fig. 7, it is suggested that upon the addition of phosphorus to the coal ash, the ash fusion temperatures were reduced through the dissolution of refractory minerals into the phosphorus-containing liquid phase formed in the initial ash melting stage, which was enhanced by the presence of Fe.

## 4. Conclusions

The effects of phosphorus on the coal ash fusion temperature were systematically investigated. Mineral transformation and refractory mineral dissolution during heating were investigated. The following conclusions are drawn.

(1) The addition of calcium or iron phosphate significantly reduced the FT of coal ash, leading to higher reduction rates compared with those obtained upon the addition of the corresponding oxides. Iron phosphate exhibited superior FT-lowering effectiveness to calcium phosphate at an equivalent additive content.

(2) The phosphorus vaporization ratio increased with the temperature. Approximately 50% of phosphorus was retained in both CaP8 and FeP8 ashes at 1400 °C. Phosphorus speciation in ash comprised $P_2O_5$ and $PO_4^{3-}$, with thermal elevation promoting conversion of $PO_4^{3-}$ into molten slag-dissolved $P_2O_5$.

(3) The phosphorus-containing liquid phase formed during the initial ash melting demonstrated an enhanced mullite

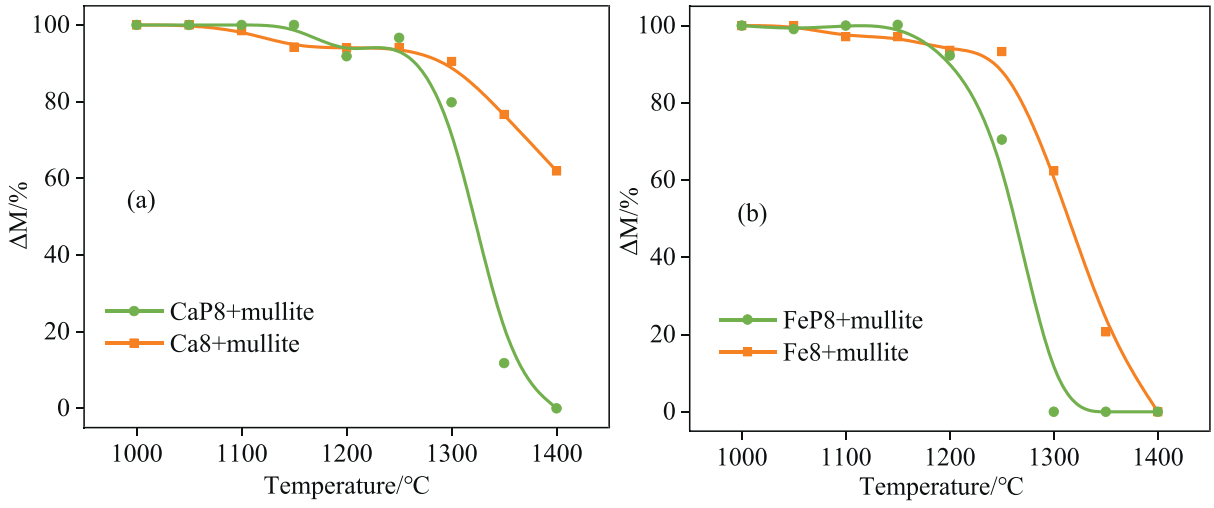


**Fig. 14.** $\Delta M$ values of mullite particles as a function of temperature.

dissolution capability compared with oxide additive systems, thereby reducing the ash FT. This dissolution capacity was further enhanced by the presence of iron.

## CRediT Authorship Contribution Statement

Guoyang Gui: Investigation, Writing – original draft, Data curation, Methodology. Facun Jiao: Writing – review & editing, Conceptualization, Methodology, Funding acquisition. Zhongbing Dong: Supervision, Methodology, Conceptualization. Yunhu Hu: Methodology, Conceptualization. Shengtao Gao: Funding acquisition, Software, Methodology. Tao Liu: Data curation, Methodology. Yuanchun Zhang: Data curation. Lirui Mao: Data curation, Software. Chengli Wu: Methodology, Conceptualization. Hanxu Li: Methodology, Conceptualization.

## Declaration of Competing Interest

The authors declare that they have no known competing financial interests or personal relationships that could have appeared to influence the work reported in this paper.

## Acknowledgements

This work was supported by the Open Research Fund Program of Engineering Technology Research Center of Coal Resources Comprehensive Utilization, Anhui University of Science and Technology (MTYJZX202203) and Anhui Key Laboratory of Low-temperature Co-fired Materials, Huainan Normal University (2022LCA02), the National Natural Science Foundation of China (52200139).

## References

[1] J. Ananda, Explaining the environmental efficiency of drinking water and wastewater utilities, *Sustain. Prod. Consum.* 17 (2019) 188–195.
[2] F.H. Li, C.Y. Zhao, H.L. Fan, M.L. Xu, Q.Q. Guo, Y. Li, L.S. Wu, T. Wang, Y.T. Fang, Ash fusion behaviors of sugarcane bagasse and its modification with sewage sludge addition, *Energy* 251 (2022) 123912.
[3] L. Batistella, V. Silva, R.C. Suzin, E. Virmond, C.A. Althoff, R.F.P.M. Moreira, H.J. José, Gaseous emissions from sewage sludge combustion in a moving bed combustor, *Waste Manag.* 46 (2015) 430–439.
[4] J.T. Feng, I.T. Burke, X.H. Chen, D.I. Stewart, Assessing metal contamination and speciation in sewage sludge: implications for soil application and environmental risk, *Rev. Environ. Sci. Biotechnol.* 22 (4) (2023) 1037–1058.
[5] H. Liu, G.J. Hu, I.A. Basar, J.B. Li, N. Lyczko, A. Nzihou, C. Eskicioglu, Phosphorus recovery from municipal sludge-derived ash and hydrochar through wet-chemical technology: a review towards sustainable waste management, *Chem. Eng. J.* 417 (2021) 129300.
[6] A.M. Zaharioiu, F. Bucura, R.E. Ionete, F. Marin, M. Constantinescu, S. Oancea, Opportunities regarding the use of technologies of energy recovery from sewage sludge, *SN Appl. Sci.* 3 (9) (2021) 775.
[7] T.P. Vo, R.C. Zhang, J. Rintala, K.K. Xiao, C. He, Effect of thermochemical treatment of sewage sludge on its phosphorus leaching efficiency: insights into leaching behavior and mechanism, *Waste Manag.* 190 (2024) 24–34.
[8] Y.J. Du, T.R. Shi, S.G. Guo, H.G. Li, Y.H. Qin, Y.F. Wang, C. He, Y.X. Wei, Unraveling the intrinsic mechanism behind the retention of arsenic in the co-gasification of coal and sewage sludge: focus on the role of Ca and Fe compounds, *J. Hazard. Mater.* 470 (2024) 134211.
[9] M.M. Ma, S.Y. Zhang, Y.N. Chen, B. Chen, L.J. Guo, Optimization of hydrogen-rich syngas from coal and sewage sludge co-gasification in supercritical water, *Chem. Eng. J.* 497 (2024) 154792.
[10] D. Schwitalla, M. Reinmöller, C. Forman, C. Wolfersdorf, M. Gootz, J. Bai, S. Guhl, M. Neuroth, B. Meyer, Ash and slag properties for co-gasification of sewage sludge and coal: an experimentally validated modeling approach, *Fuel Process. Technol.* 175 (2018) 1–9.
[11] C.L. Wu, Y. Xin, X. Liu, H.X. Li, F.C. Jiao, Synergistic effect of CaO and MgO addition on coal ash fusibility in a reducing atmosphere, *Asia Pac. J. Chem. Eng.* 14 (4) (2019) e2324.
[12] C. He, J. Bai, A. Ilyushechkin, H.L. Zhao, L.X. Kong, H.Z. Li, Z.Q. Bai, Z.X. Guo, W. Li, Effect of chemical composition on the fusion behaviour of synthetic high-iron coal ash, *Fuel* 253 (2019) 1465–1472.
[13] W. Zhao, L.M. Zhang, X.D. Song, Y.C. Li, C.Y. Zhao, J.T. Wei, Y.H. Bai, P. Lv, W.G. Su, G.S. Yu, Effect of residual carbon on the flow properties of iron-containing coal ash: Ash fusibility and viscosity-temperature characteristics, *Fuel* 374 (2024) 132467.
[14] Q. Zhang, H.F. Liu, Y.P. Qian, M.H. Xu, W.F. Li, J.L. Xu, The influence of phosphorus on ash fusion temperature of sludge and coal, *Fuel Process. Technol.* 110 (2013) 218–226.
[15] H. Wu, X. Liu, X. Cao, Q.H. Guo, G.S. Yu, Effects of phosphorus on the fusion characteristics of synthetic ashes with different $Al_2O_3$/CaO ratios, *Fuel* 361 (2024) 130698.
[16] X.X. Zhang, H.Y. Dou, J. Bai, L.X. Kong, W. Feng, H.Z. Li, Z.X. Guo, Z.Q. Bai, P. Li, W. Li, Effect of phosphorus on viscosity-temperature behavior of high-sodium coal ash slag, *Fuel* 343 (2023) 127930.
[17] H. Wu, X. Cao, Q.H. Guo, X. Liu, G.S. Yu, Effects of phosphorus pentoxide on viscosity-temperature characteristics of sewage sludge ash slags under mild reducing atmosphere, *Fuel* 376 (2024) 132763.
[18] C. He, Y.J. Du, X.R. Cai, J.R. Wang, Y.H. Qin, Z.B. Zhao, H.Z. Li, S.V. Vassilev, C.G. Vassileva, *In-situ* analysis of the sintering behavior of coal ash and a phosphorus-rich biomass ash under gasification condition, *Biomass Bioenergy* 168 (2023) 106671.
[19] X.X. Zhang, J. Bai, S.V. Vassilev, L.X. Kong, L. Huang, H.Z. Li, Z.Q. Bai, P. Li, W. Li, Effect of phosphorus-based additives on ash fusion characteristics of high-sodium coal under gasification condition, *Fuel* 317 (2022) 123472.
[20] J.G. Shao, D.H. Lee, R. Yan, M. Liu, X.L. Wang, D.T. Liang, T.J. White, H.P. Chen, Agglomeration characteristics of sludge combustion in a bench-scale fluidized bed combustor, *Energy Fuels* 21 (5) (2007) 2608–2614.
[21] J. Bedia, V.M. Monsalvo, J.J. Rodriguez, A.F. Mohedano, Iron catalysts by chemical activation of sewage sludge with $FeCl_3$ for CWPO, *Chem. Eng. J.* 318 (2017) 224–230.
[22] Y.L. Zhang, Y.L. Shi, B. Yan, F.P. Zhang, S.T. Wang, C.C. Fan, L. Chen, X.L. Xu, X. H. Guo, A novel iron-based composite flocculant for enhanced wastewater treatment and upcycling hazardous sludge into trifunctional electrocatalyst, *Appl. Surf. Sci.* 569 (2021) 151034.
[23] F.H. Li, H.L. Fan, X.C. Wang, T. Wang, Y.T. Fang, Influences of phosphorus on ash fusion characteristics of coal and its regulation mechanism, *Fuel* 239 (2019) 1338–1350.
[24] Y.P. Yu, Z.A. Yu, W. Xu, K.B. Zhang, Y.N. Tang, G.J. Cheng, X. He, B.Q. Dai, High-temperature ash melting and fluidity behavior upon the cocombustion of sewage sludge and coal, *ACS Omega* 9 (12) (2024) 14455–14464.
[25] H. Wu, J.J. Wang, X. Liu, X. Cao, Q.H. Guo, G.S. Yu, Effects of phosphorous-based additive on flow properties of high silicon-aluminum coal ash, *Fuel* 328 (2022) 125238.
[26] M. Li, F.H. Li, Q.R. Liu, Y.T. Fang, H.X. Xiao, Regulation of ash fusibility for high ash-fusion-temperature (AFT) coal by industrial sludge addition, *Fuel* 244 (2019) 91–103.
[27] S.V. Vassilev, D. Baxter, C.G. Vassileva, An overview of the behaviour of biomass during combustion: Part II. Ash fusion and ash formation mechanisms of biomass types, *Fuel* 117 (2014) 152–183.
[28] H.L. Liang, J.H. Yi, Y. Yang, L. Zhang, T. Ma, W.B. Chen, H. Liu, D.F. Che, Study on the mechanism of multiple sodium salts co-loading on ash fusibility and mineral evolution behaviors, *Fuel* 397 (2025) 135397.
[29] Z.Q. Yang, F.H. Li, M.J. Ma, W. Zhao, X.F. Liu, Y. Wang, Z.Z. Li, Y.T. Fang, Effecting mechanisms of iron-rich sludge on ash fusion characteristics of coal with high ash fusion temperature under reducing atmosphere, *Waste Manag.* 174 (2024) 328–339.
[30] X. Cao, Z.F. Ge, X. Liu, H. Wu, G.S. Yu, Comprehensive analysis on the *in situ* ash fusibility and mineral reactions of ash mixtures in the co-gasification process, *Fuel Process. Technol.* 241 (2023) 107589.
[31] H.X. Li, J.Y. Xiong, Y.X. Tang, X. Cao, Mineralogy study of the effect of iron-bearing minerals on coal ash slagging during a high-temperature reducing atmosphere, *Energy Fuels* 29 (11) (2015) 6948–6955.
[32] Y.J. Wei, H.X. Li, N. Yamada, A. Sato, Y. Ninomiya, K. Honma, T. Tanosaki, A microscopic study of the precipitation of metallic iron in slag from iron-rich coal during high temperature gasification, *Fuel* 103 (2013) 101–110.
[33] Z.J. Shen, Q.F. Liang, B.B. Zhang, J.L. Xu, H.F. Liu, Effect of continuous cooling on the crystallization process and crystal compositions of iron-rich coal slag, *Energy Fuels* 29 (6) (2015) 3640–3648.
[34] L.X. Kong, J. Bai, Z.Q. Bai, Z.X. Guo, W. Li, Effects of $CaCO_3$ on slag flow properties at high temperatures, *Fuel* 109 (2013) 76–85.
[35] X.X. Zhang, L. Huang, X.W. Bai, W. Feng, J. Bai, L.X. Kong, Z.Q. Bai, M. Zhong, Z. H. Dai, W. Li, The effect of sewage sludge on Zhundong coal ash melting behavior under different atmosphere, *Mater. Chem. Phys.* 333 (2025) 130396.